Dynamic Stability of a Mobile Manipulating Unmanned Aerial Vehicle

Christopher Korpela, Matko Orsag, Miles Pekala, and Paul Oh

***Abstract*— This paper presents a control scheme to achieve dynamic stability in an aerial vehicle with dual multi-degree of freedom manipulators. Arm movements assist with stability and recovery for ground robots, in particular humanoids and dynamically balancing vehicles. However, there is little work in aerial robotics where the manipulators themselves facilitate flight stability or the load mass is repositioned in flight for added control. We present recent results in arm motions that achieve increased flight stability without and with different load masses attached to the end-effectors. Our test flight results indicate that we can accurately model and control our aerial vehicle when both moving the manipulators and interacting with target objects.**

I. Introduction

In recent years, robots that rely on dynamic control techniques for movement or manipulation have become increasingly prevalent. Robotic systems of this type involve challenging control problems due in part to the fact that a robot's base and it's manipulators may be dynamically coupled. For dynamically balancing robots, robots with flexible bases, or humanoids, base reactions created by the vehicle's manipulator may be significant enough to warrant active reduction or compensation to maintain stability. Previous work with ground systems has shown that if vibration suppression control is not correctly handled it can lead to destabilizing effects [1]. Additionally, others have analyzed arm recovery motions to reduce the impact on a dynamically stable base vehicle [2]. Similar work with humanoids has been done involving balancing during manipulation or grasping for added stability [3].

Although work has been done in this area with ground-based vehicles, little work has been done in aerial vehicles where arm or manipulator motions may lead to decreased stability and control problems. There have been recent attempts in aerial grasping using a 1-DOF (degree of freedom) grasper or gripper [4], [5], [6]. Other groups have introduced gimbals [7], suspended payload [8], force sensors [9], or brushes [10] attached to quadrotors or duct-fan vehicles where the manipulator is used for contact inspection. The AIRobots consortium [11] is also developing service robots for use in hazardous or unreachable locations. Previous work from the authors has produced a prototype 3-arm aerial manipulator in addition to a miniature test and evaluation quadrotor emulation system [12], [13].

Manuscript received September 17, 2012. This project was supported in part by a US NSF PIRE Grant 0730206 and US NSF CAREER Grant 0347430.

C. Korpela and P. Oh are with the Drexel Autonomous Systems Lab, Drexel Univeristy, Philadelphia, PA 19104 USA cmk325@drexel.edu, paul@coe.drexel.edu

M. Orsag is with Faculty of Electrical Engineering and Computing, University of Zagreb, 10000 Zagreb, Croatia morsag@fer.unizg.hr

M. Pekala is with Motile Robotics Inc., Joppa, MD 21085 USA miles.pekala@motilerobotics.com

Fig. 1: MM-UAV carrying a long rod

It is apparent that compensation of reactionary forces caused during manipulation or manipulator movement is critical to robust control of an aerial vehicle. Reaction forces observed during arm movement and those caused by ground contact introduce destabilizing effects into an already inherently unstable system. Novel control architectures for flight and arm dynamics are required to maintain stability during manipulation and flight. However, aerial grasping and manipulation still remains largely underdeveloped. This fact is mostly due to poor payload capabilities available from micro UAVs in addition to the possibility of crashing and causing injury.

This paper presents a tightly coupled dynamic and kinematic model for a mobile manipulating unmanned aerial vehicle, dubbed MM-UAV, as shown in Fig. 1 and described in Sections II and III. Stability analysis (Sec. IV) is performed on the model to develop permissible arm movements that do not violate flight stability regions. The model and control architecture are implemented in both simulation (Sec. V) and hardware (Sec. VI) to characterize and compensate for reactionary forces. The end-effector pose for each arm (2 total) is a combination of the six DOFs of the quadrotor and the four DOFs for each respective arm for a total of 16 degrees of freedom. The aerial manipulation system presented in this paper can successfully grasp and transport various objects while maintaining stable flight.

II. Manipulator Model

A. Manipulator Kinematics

Forward kinematics for the two serial chain manipulators are derived using Denavit-Hartenberg (DH) parameters as

Link	θ	d	a	α
B-0	$\frac{\pi}{2}$	d_b	a_b	0
0	0	0	0	0
1	$q_A^1 - \frac{\pi}{2}$	0	3.75	$-\frac{\pi}{2}$
2	q_A^2	0	3.75	$\frac{\pi}{2}$
3	q_A^3	0	3.75	$-\frac{\pi}{2}$
4	$q_A^4 + \frac{\pi}{2}$	0	0	$\frac{\pi}{2}$
T-E	0	0	3.75	0

TABLE I: Denavit-Hartenberg Parameters for Manipulators $[cm]$. Showing Arm A only for clarity.

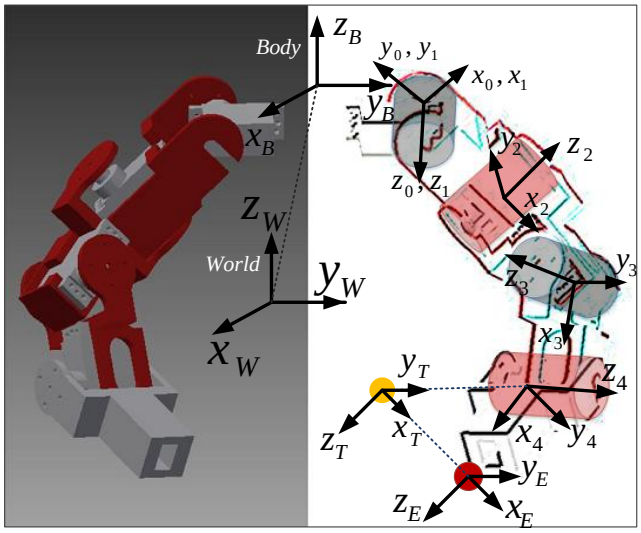

Fig. 2: Reference Frames for Manipulator Arms

shown in Table I. Parameters θ, d, a, and α are in standard DH convention and q_i^1, q_i^2, q_i^3, and q_i^4 are joint variables of each manipulator arm $i = [A, B]$. Both arms are symmetrical and offset equally from the vehicle's geometric center. Since the general kinematic structure is identical for the right and left arms, the coordinate frames are the same for each arm, only the link B-0 is different. Reference frames are shown in Fig. 2 which relate the inertial or world frame, W, to the vehicle or body frame, B, to the tool or end-effector frame, E. To make the DH parameters consistent, an additional frame T is set in the origin of frame L_4. The direct kinematics function relating the quadrotor body to the end-effector frame is obtained by chain-multiplying the transformation matrices together:

$$T_b^e(q) = T_b^0 T_0^4 T_4^e \tag{1}$$

The two constant homogeneous transformation matrices describing the position and orientation of Frame 0 *w.r.t.* the body frame and Frame 4 *w.r.t.* the end-effector frame have the form:

$$T_0^b = \begin{bmatrix} 0 & 0 & 1 & 0 \\ 1 & 0 & 0 & a_b \\ 0 & 1 & 0 & d_b \\ 0 & 0 & 0 & 1 \end{bmatrix} \tag{2a}$$

$$T_e^4 = \begin{bmatrix} 0 & 0 & 1 & 0 \\ 0 & 1 & 0 & 0 \\ -1 & 0 & 0 & 0 \\ 0 & 0 & 0 & 1 \end{bmatrix} \tag{2b}$$

and intermediate transformations for each joint are:

$$A_0^1(q_1) = \begin{bmatrix} c_{\theta_1} & 0 & s_{\theta_1} & a_1 c_{\theta_1} \\ s_{\theta_1} & 0 & c_{\theta_1} & a_1 s_{\theta_1} \\ 0 & -1 & 0 & 0 \\ 0 & 0 & 0 & 1 \end{bmatrix} \tag{3a}$$

$$A_1^2(q_2) = \begin{bmatrix} c_{\theta_2} & 0 & s_{\theta_2} & a_2 c_{\theta_2} \\ s_{\theta_2} & 0 & -c_{\theta_2} & a_2 s_{\theta_2} \\ 0 & 1 & 0 & 0 \\ 0 & 0 & 0 & 1 \end{bmatrix} \tag{3b}$$

$$A_2^3(q_3) = \begin{bmatrix} c_{\theta_3} & 0 & s_{\theta_3} & a_3 c_{\theta_3} \\ s_{\theta_3} & 0 & c_{\theta_3} & a_3 s_{\theta_3} \\ 0 & -1 & 0 & 0 \\ 0 & 0 & 0 & 1 \end{bmatrix} \tag{3c}$$

$$A_3^4(q_4) = \begin{bmatrix} c_{\theta_4} & 0 & s_{\theta_4} & a_4 c_{\theta_4} \\ s_{\theta_4} & 0 & -c_{\theta_4} & a_4 s_{\theta_4} \\ 0 & 1 & 0 & 0 \\ 0 & 0 & 0 & 1 \end{bmatrix} \tag{3d}$$

where

$$T_0^4(q) = A_0^1 A_1^2 A_2^3 A_3^4 \tag{4}$$

represents the cumulative transformation for the four joints of each manipulator. To account for quadrotor position and orientation with respect to the world frame W, an additional matrix multiplication has to be made with a 6-DOF Euler transformation matrix T_W^B.

B. Manipulator Dynamics

Using the recursive Newton-Euler approach, each arm is modeled as a serial chain RRRR manipulator. The quadrotor body frame is first modeled as a static revolute joint with a constant angular offset for each MM-UAV arm (Link B-0). Equations can easily be augmented to account for the mobile base by adding quadrotor dynamics to the base frame [14]. In this paper, forces and torques are viewed from the quadrotor body frame in which the low level attitude controller stabilizes the aircraft [12].

With Denavit-Hartenberg parameterization, joint frames are set and direct kinematics equations for each serial chain are derived. This procedure is repeated for both manipulator arms. Given the initial angular Ω_B and translational V_B velocities of the quadrotor body, the angular $\vec{\omega}_j^i$ and translational $\vec{v}_j^i$ velocities and the derivatives of the velocity vectors (i.e. $\dot{v}_j^i$ and $\dot{\omega}_j^i$) for each joint j and each arm i, can be propagated and expressed in the quadrotor body frame. After forward step calculations of joint speeds and accelerations, applying Newton-Euler laws obtains the necessary force and torque equations.

III. Quadrotor Model

A. Quadrotor Dynamics

The focus of this paper is to show how manipulator dynamics influence the dynamics of the quadrotor. As such, quadrotor dynamics considered in this paper do not account for various aerodynamic effects (i.e. blade flapping, ground effect, etc.) experienced during highly dynamic flying maneuvers. Most of the vehicle's critical motions occur around hover outside of ground effect. This fact justifies a simplified mathematical model since with given speeds and maneuverability, the quadrotor experiences little to none of the previously mentioned aerodynamic effects.

The quadrotor dynamic model begins with Newton-Euler equations for rigid body translation and rotation [15]. Because the mobile manipulator dynamics are introduced through the recursive Newton-Euler method, it is possible to consider the quadrotor motion as separate from the manipulator. Manipulator mass, moments of inertia, and movement are later calculated and regarded as disturbances to the quadrotor model.

$$\begin{bmatrix} F_q \\ \tau_q \end{bmatrix} = \begin{bmatrix} m_q \mathbf{I} & 0 \\ 0 & \mathbf{J}_q \end{bmatrix} \begin{bmatrix} \vec{v} \\ \dot{\vec{\omega}} \end{bmatrix} + \begin{bmatrix} 0 \\ \vec{\omega}_q \times \mathbf{J}_q \vec{\omega}_q \end{bmatrix} \tag{5}$$

The second key part of quadrotor dynamics is the propulsion system torque and thrust. With no additional aerodynamic effects, propeller thrust and drag can be estimated using the NACA-standardized thrust and torque coefficients C_T (6a) and C_Q (6b). In [16], the authors measured the performance of various propellers used in UAVs. Knowing the thrust and torque coefficients of given propellers, one can easily calculate the thrust and torque of each propeller with respect to applied voltage.

$$C_T = \frac{T}{\rho n^2 D^4} \tag{6a}$$

$$C_Q = \frac{Q}{\rho n^2 D^5} \tag{6b}$$

Rotor thrust and torque are marked T and Q, respectively; ρ stands for air density which is assumed to be constant; $n \propto U[V]$ is the rotor speed; and D is the rotor radius. Forces and torques of each propeller are added according to standard quadrotor propulsion system equations as shown in (7).

$$\begin{aligned} \vec{F_{tot}} &= \vec{T^1} + \vec{T^2} + \vec{T^3} + \vec{T^4} \\ \tau_x^{tot} &= \tau_x^2 + \tau_x^3 - \tau_x^1 - \tau_x^4 \\ \tau_y^{tot} &= \tau_y^3 + \tau_y^4 - \tau_y^1 - \tau_y^2 \\ \tau_z^{tot} &= \tau_z^2 + \tau_z^4 - \tau_z^1 - \tau_z^3 \end{aligned} \tag{7}$$

Dynamics of brushless DC motors used on the aircraft proved to have an important impact in aircraft stability and cannot be omitted from the MM-UAV model. Off the shelf electronic speed controllers are used to power and control the motors, which makes it impossible to devise a complete model for the motors. Therefore, a simplified 1st order PT1 dynamic model is used.

Considering simplified aerodynamic conditions, propellers simply produce thrust forces T^i as shown in (6a). Summing them all together gives the total aircraft thrust. Each propeller torque τ^i, in contrast, has two components, one coming from the actual propeller drag (6b), and the other due to the displacement of the propeller from the COG.

$$\vec{\tau}^i = \vec{Q}^i + \Delta \vec{R}_T^i \times \vec{T}^i \tag{8}$$

IV. Stability Analysis

Given the dynamic model for both manipulators and the quadrotor body, a simplified arm model is utilized to establish stability criteria for the complete system. Much of the previous work in quadrotor flight and stability assumes the geometric center and quadrotor center of mass are coincident. In our model as shown in Figs. 3a and 3b, the quadrotor center of mass Q_{CM} is shown offset downward in the z direction due to the mass of the arms. Further, the overall center of mass, CM, shifts based on the joint angles of the two shoulder joints.

Previous work in aircraft stability analysis has measured center of mass offsets based on the load mass while ignoring affects from the gripper [4], [5]. In this work, the 4-DOF arms and end-effectors introduce a significant increase in payload and disturbance to the dynamics and therefore cannot be neglected.

A. Simplified Kinematics

In this simplified kinematics model (Figs. 3a and 3b), only the movement of the first two arm joints are analyzed (i.e. q_A^1, q_A^2, q_B^1, and q_B^2). The remainder of the arm joints remain fixed. This simplification allows us to view the arms as links of length $2C_1$, $2C_2$ and mass m_A^1, m_B^2 respectively, and corresponding moments of inertia:

$$I = \frac{mC^2}{12} cos(\Theta)^2 \tag{9}$$

with Θ marking the angle between the axis of rotation and link C. Key aspects observed are the changes in roll and pitch angle dynamics. This analysis could later be easily applied to yaw angle stability. Both figures show how the arms A and B movements affect rolling and pitching angle accelerations $\dot{\omega}_y$ and $\dot{\omega}_x$. One can easily calculate the varying center of mass CM:

$$CM = \frac{Q_{cm} m_Q + A_{cm} m_A + B_{cm} m_A}{m_Q + 2m_A} \tag{10}$$

as a function of varying vector distances of link centers of mass A_{cm} and B_{cm}, a constant vector quadrotor center of mass Q_{cm} and link masses $m_A = m_B$ together with quadrotor mass m_Q. Vectors A_{cm} and B_{cm} change as joints q_A^1, q_B^1 and q_A^2, q_B^2 move. Analyzing the two situations separately, the equations for these vectors can be derived:

$$A_{cm} = \left[D - C_1 sin(q_A^1)\right] \hat{x} + \left[L_1 + C_1 cos\left(q_A^1\right)\right] \hat{z} \tag{11a}$$

$$B_{cm} = \left[C_1 sin(q_B^1) - D\right] \hat{x} + \left[L_1 + C_1 cos\left(q_B^1\right)\right] \hat{z} \tag{11b}$$

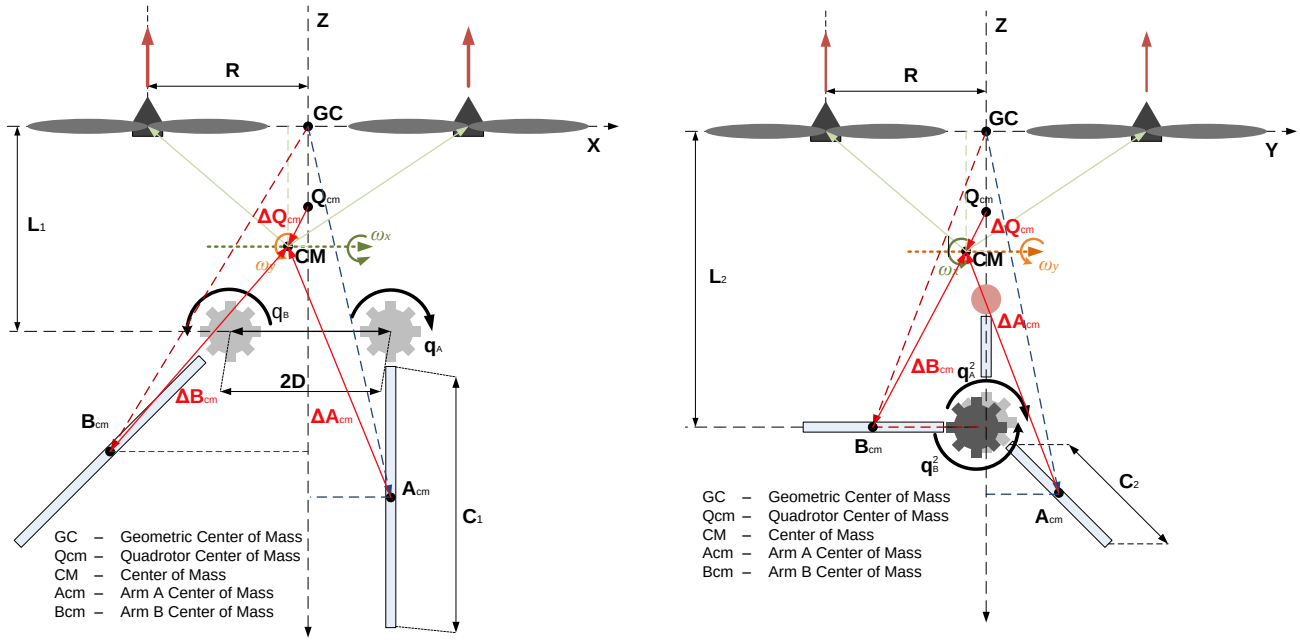

(a) Joint 1

(b) Joint 2

Fig. 3: Simplified Arm Model

$$A_{cm} = -D\hat{x} + \left[-C_2 sin(q_A^2)\right]\hat{y} + \left[L_2 + C_2 cos\left(q_A^2\right)\right]\hat{z} \tag{11c}$$

$$B_{cm} = D\hat{x} + \left[C_2 sin(q_B^2)\right]\hat{y} + \left[L_2 + C_2 cos\left(q_B^2\right)\right]\hat{z} \tag{11d}$$

where the constant dimensions D, L_1 and L_2 are marked in Figs. 3a and 3b). The equations show how in these two situations, movements of joints 1 and 2 have a very same mathematical representation. This leads to the conclusion that the final equations will have a similar form.

The overall moment of inertia CM changes as the joints move. This variation can easily be derived using the Parallel axis theorem:

$$\begin{aligned} I_{cm} &= I_Q + I_A + I_B + \\ &+ m_Q \Delta Q^2 + m_A \Delta A^2 + m_B \Delta B^2 \end{aligned} \tag{12}$$

Where $\Delta Q, \Delta A$ and ΔB represent the center of mass of each body with respect to the overall center of mass CM.

$$\Delta Q = \frac{m_A \left(A_{cm} + B_{cm} - 2Q_{cm}\right)}{m_Q + 2m_A} \tag{13a}$$

$$\Delta A = \frac{m_Q \left(Q_{cm} - A_{cm}\right) + m_A \left(B_{cm} - A_{cm}\right)}{m_Q + 2m_A} \tag{13b}$$

$$\Delta B = \frac{m_Q \left(Q_{cm} - B_{cm}\right) + m_A \left(A_{cm} - B_{cm}\right)}{m_Q + 2m_A} \tag{13c}$$

Final equations for CM moment of inertia are too complex to be presented in analytic form, therefore the overall changes in I_{CM} are shown in Fig 4. The images are plotted relative to the quadrotor moment of inertia I_Q. Although the effects of each joint change are similar, there are a few substantial differences: Joints 1 cause a greater shift in CM then Joints 2, due to the fact that they carry longer part of the MM-UAV arms; Furthermore, Joints 1 cause opposite effects on I_{xx} and I_{yy}. With the arms in a horizontal position ($q_A^1 = q_B^1 = -90°$), I_{yy} increases, while I_{xx} following (9) decreases; Because the joints are perpendicular to each other, their effects are reversed; Joints 2 have a slightly larger operating range (i.e. 180° instead of 120°); Finally, we conclude that Joints 2 have a similar effect on both moments of inertia, increasing them when the arms are fully extended downwards. The biggest effect is observed on the y axis when Joints 1 move, and the biggest variations in moment of inertia are observed on the x axis, when Joints 1 move.

B. Angle Control Stability

Control of the MM-UAV body is achieved through PI-D control shown in Fig. 5. This form of PID control was chosen because it eliminates potential damages to the actuators that can usually be experienced when leading the control difference directly through the derivation channel [17]. In order to analyze the stability of the system, one needs to know the varying parameters in the control loop. The disturbance caused from the Euler equation component $\omega_y \omega_z (I_{yy} - I_{zz})$ affects the behavior of the control loop, but not its stability and therefore will not be considered in this analysis. The major factor that affects the stability of the aircraft is the moment of inertia $J = I_x x, I_y y$. Mathematical formalisms that describe the variations in the moment of inertia was given in Sec. IV-A.

The transfer function of the angle control loop in Fig. 5 can easily be derived (14). Similarly as in [5], the stability conditions are applied to its 4th order characteristic polyno-

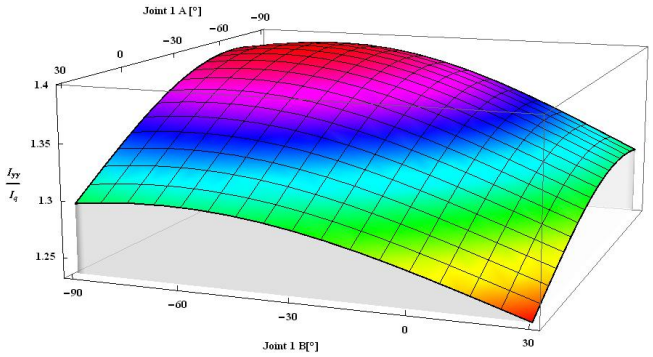

(a) I_{yy} Joints 1A and 1B

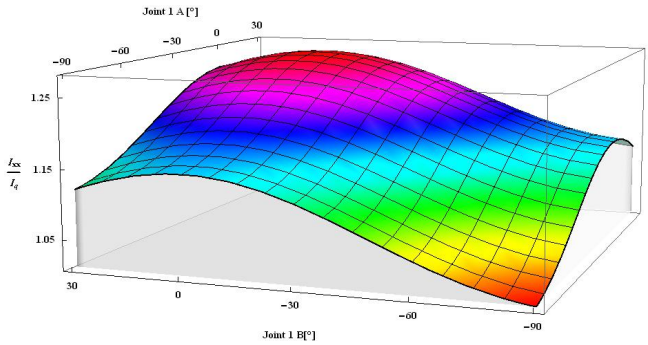

(b) I_{xx} Joints 1A and 1B

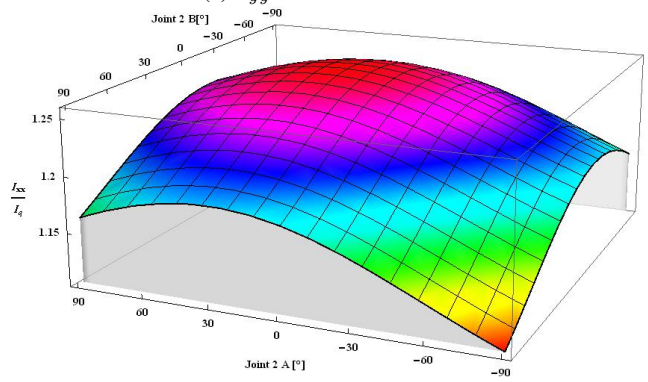

(c) I_{yy} Joints 2A and 2B

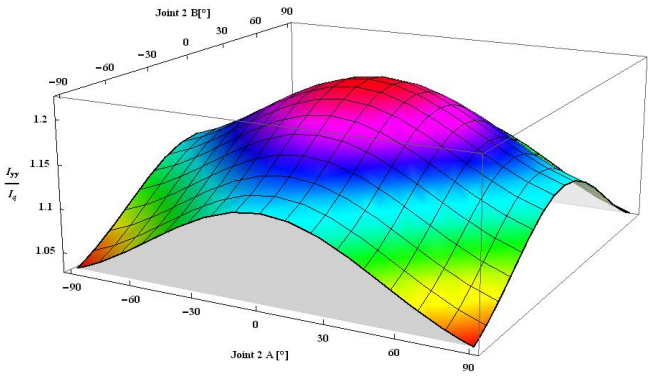

(d) I_{xx} Joints 2A and 2B

Fig. 4: Moments of inertia variations with respect to joint angle changes.

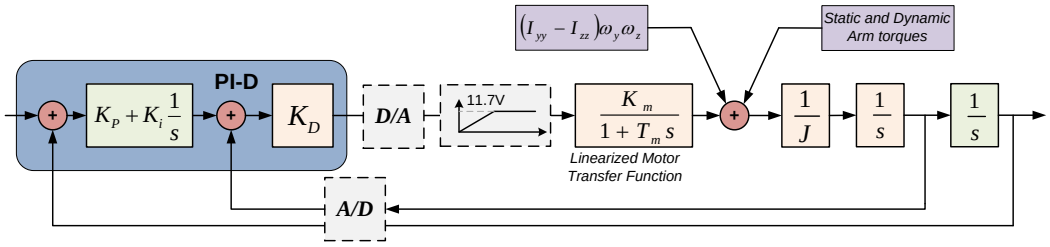

Fig. 5: Joint Angle Control

mial $a_4s^4 + a_3s^3 + a_2s^2 + a_1s + a_0$, where the 4th order dynamic system includes both the dynamics of the aircraft and motor dynamics.

$$G_{\alpha_{CL}} = \frac{\frac{K_D K_m}{K_i T_m J}\left(\frac{K_p}{K_i}s + 1\right)}{s^4 + \frac{1}{T_m}s^3 + \frac{K_D K_m}{T_m J}s^2 + \frac{K_d K_m K_p}{T_m J}s + \frac{K_d K_m K_i}{T_m J}} \tag{14}$$

Coefficients K_D, K_p and K_i are PI-D respective gains and K_m and T_m represent propulsion system gain and motor time constant. If we apply the Routh-Hurwitz stability criteria, it is possible to derive the analytical equations for stability conditions. The necessary system stability conditions require that all coefficients be positive and that inequalities in (15) are satisfied. Stability criteria (15) shows that, due to the dynamics introduced from the motors (i.e. T_m), the proportional control K_p can drive the system unstable. In fact, only the derivative control K_d has the sole purpose of stabilizing the system. This shows how the motor dynamics cannot be neglected when analyzing MM-UAV stability.

$$\frac{K_d K_m K_p}{K_i}\left(1 - T_m K_p\right) > J \tag{15a}$$

$$K_d K_m \left(1 - T_m K_p\right) > 0 \tag{15b}$$

Moreover, the angle control loop in Fig. 5 can be observed as a cascade system, where the K_D gain serves as inner loop controller. This approach enables tuning the PI-D controller in two separate steps (i.e. rotation speed and angle loop). After closing the speed loop, the inner loop transfer function takes the standard 2nd order transfer function form:

$$G_{\omega_{CL}} = \frac{1}{1 + \frac{J}{K_D K_m}s + \frac{J T_m}{K_D K_m}s^2} \tag{16}$$

It can further be shown that the equations for the system's

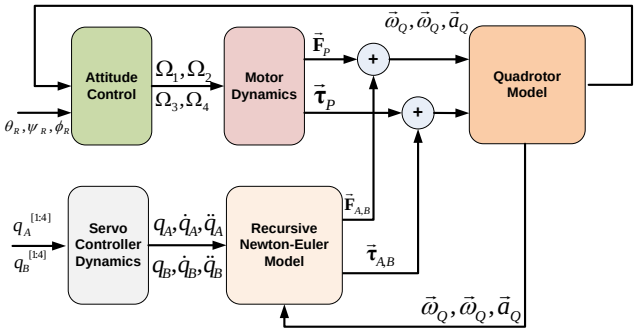

Fig. 6: Simulation Scheme

natural frequency ω_n and damping ratio ζ are:

$$\omega_n = \sqrt{\frac{K_D K_m}{J T_m}} \tag{17a}$$

$$\zeta = \frac{1}{2}\sqrt{\frac{J}{K_D K_m T_m}} \tag{17b}$$

While from (15) follows that a smaller moment of inertia increases the system stability, (17) shows that smaller moments of inertia cause oscillations in the inner loop. While that is not a problem in this analysis, in the actual implementation, where a discrete form and input limits are used, the amplitude and frequency of these oscillations can cause serious problems and stability issues. The amplitude can causes problems when faced with control inputs limits (i.e. $12V$) and the frequency is of concern when it surpasses the sampling frequencies. Smaller moments of inertia produce higher frequencies and smaller damping ratios thus can decrease the stability in multiple ways.

V. Simulation

The simulation model for MM-UAV must incorporate quadrotor dynamics and propeller aerodynamics from Sec. III, together with a complete dynamic model of the arms (Sec. II), controlling the system with a PI-D controller from Sec. IV. Figure 6 shows the layout for the simulation model used in this paper. The attitude controller takes angle reference values and quadrotor feedback signals as input. A PI-D algorithm then calculates the necessary rotor speeds that power the propeller dynamics block that produces respective torques and forces applied to the body. A recursive Newton-Euler dynamic model is used to model the arms as a disturbance to the quadrotor control loop. This recursive model calculates the torques and forces based on movements of the arms and quadrotor dynamics. Arm movement is modeled through a PT2 dynamic system, tuned with the technical optimum criteria, that emulates expected servo motor dynamics. Matlab was used for simulations and a recursive Newton-Euler dynamics model of the manipulators was implemented using the Robotics Toolbox [18].

In order to test the proposed stability analysis, a series of simulation tests were run. Figures 7 and 8 show the results

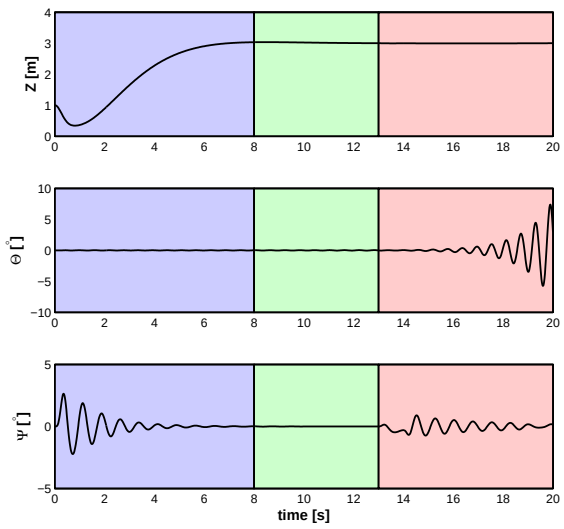

Fig. 7: Matlab Simulation (Take off with arms stowed, Oscillations settled; Deploying arms move): Roll and pitch angles

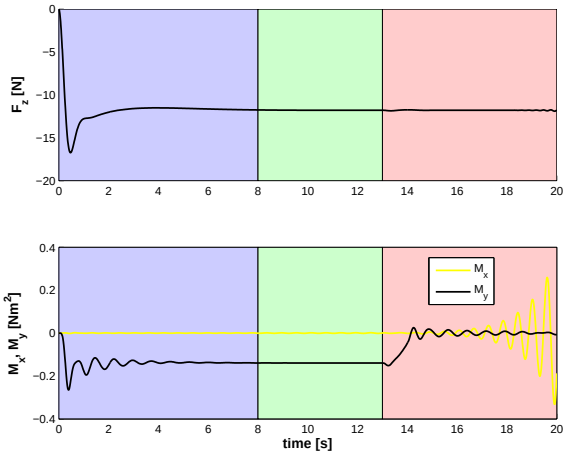

Fig. 8: Matlab Simulation (Take off with arms stowed, Oscillations settled; Deploying arms move): Propulsion system thrust and torque values

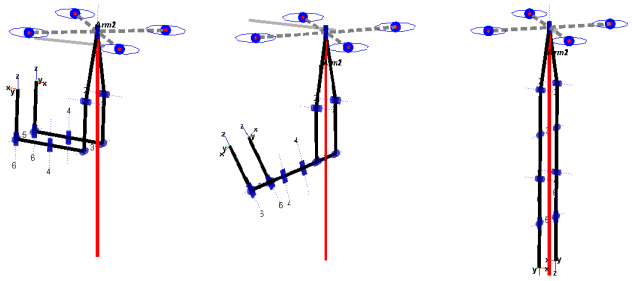

Fig. 9: Left to right, MM-UAV arm transition from stowed to fully deployed

of one of these tests. In this particular test, the quadrotor roll controller was tuned close to the stability boundary. The aircraft takes off with arms tucked and stowed. After the vehicles settles to a hover, the arms are deployed down and fully extended (Fig. 9), thus increasing the moments of inertia. This movement causes the roll angle control to become unstable, which can be seen in the red portion of Fig. 7. The pitch controller, on the other hand, is tuned closer to the safe, stable controller region, and thus does not become unstable. It does, however, exhibit more oscillatory behavior, due to the increase of its moment of inertia. Figure 8 shows the rotors forces and torques from this experiment. It is interesting to notice how the controller compensates for the additional torque load at the beginning of the experiment. This load is caused by the arms' center of mass positioned away from the Q_{CM}. This causes static torque on the quadrotor body, which the integral component of the PI-D controller compensates. Once the arms are extended downward, this torque disappears as the arms' center of mass are closer to Q_{CM}.

VI. Experimental Results

A. Hardware Design

The MM-UAV vehicle is constructed using a low-cost quadrotor aircraft (GAUI 500X) and two manipulator arms. The GAUI quadrotor uses four equally positioned 960 kV brushless motors equipped with 10 inch propellers to provide lift and maneuverability. The vehicle diameter is 500mm and the aircraft is capable of lifting objects below 500g. A landing gear system, originally designed for a pan-tilt camera, has been modified to provide an unobstructed workspace for the manipulators. Each manipulator consists of 4 DOFs with a single DOF parallel-gripper end-effector. Joints are actuated using micro servos: a Hitec HS-85BB servo for the shoulder joint and HS-65MG servos for the upper and lower elbows, wrist, and gripper. The parallel gripper provides a relatively high amount of holding force compared to its small size. The arms were constructed using 3D printed polycarbonate linkages that are extremely lightweight (less than 10g each). Each joint is twisted 90 degrees to allow greater manipulator strength and reachability. Each arm including servos weighs less than 100g with a total weight of 200g for the assembly. The human operator has the option of several pre-determined poses used for take-off, landing, and during object manipulation. Final construction is shown in Fig. 1.

B. Test Setup

An off-the-shelf IMU (inertial measurement unit) fused with motion capture data is used to control the yaw, pitch, and roll of the quadrotor. Indirect Kalman filtering is used to fuse gyroscopic sensor data and motion capture visual feedback data. Low-level control is implemented on an Arducopter board that runs Kalman filtering and a PI-D controller loop with a $50Hz$ sample rate. Motion capture is based on vision markers placed just above the center of mass of the vehicle. An operator controls both the quadrotor and arms using a joystick that provides position control of the air vehicle and joint control of the servos. A ROS-based PC program routes available motion capture data (i.e. x, y, z position and speed) and joystick data to the Arducopter board using rosserial. The motion capture system used in this research is based on 18 V100:R2 OptiTrack cameras connected to a separate PC running Arena Software.

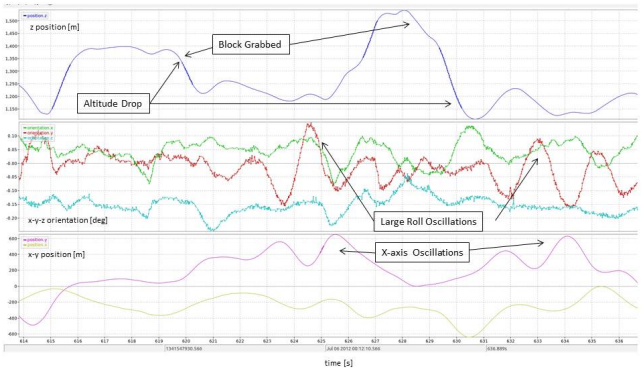

Fig. 10: Grab and Drop

C. Flight Tests

In this section, the results of three different experiments are presented: unladen flight with arm articulation, long cylinder grab and curl, and foam block grab and drop. Following lift-off under manual control, the autopilot is enabled. The operator can move the aircraft to achieve a suitable hover location in addition to changing arms from a stow position to grab posture. The first experiment demonstrates changes to vehicle pitch and roll angles over time when the arms are articulated up and down without a load mass attached. The second experiment demonstrates grasping onto a long cylindrical rod and performing "curling" style movements where the rod is moved in an up and down motion. The last experiment consists of a grab and drop of a foam block. The arms are used to clamp the block, the aircraft moves to a desired location, and the block is released (Fig. 10). In this experiment, when the block is grabbed, the vehicle drops in altitude and shows oscillations along the x axis. Once the block is released, the vehicle stabilizes and gains in altitude. The second peak in Fig. 10 demonstrates the same behavior. Refer to the attached video for flight test experiments.

VII. Conclusions

In this paper a multi-arm manipulating aerial vehicle using a small, off-the-shelf quadrotor is presented. One of the goals of this research is to further push the field of UAV research towards aerial mobile manipulation. The system kinematics and dynamics have been applied to our controller implementation to compensate for reactionary forces during arm movement. Through stability analysis, we have identified manipulator joint positions that ensure flight stability for a simple PI-D controller. Flight tests and simulation results

confirm the kinematic and dynamic model and controller for the system. In the future, we plan to test different adaptive and robust control techniques in order to achieve greater flight stability and more dexterous manipulation.

REFERENCES

[1] T. Wimbock, D. Nenchev, A. Albu-Schaffer, and G. Hirzinger, "Experimental study on dynamic reactionless motions with dlr's humanoid robot justin," in *Proc. IEEE/RSJ Int. Conf. Intelligent Robots and Systems IROS 2009*, 2009, pp. 5481–5486.

[2] S. Kuindersma, R. Grupen, and A. Barto, "Learning dynamic arm motions for postural recovery," in *Humanoid Robots (Humanoids), 2011 11th IEEE-RAS International Conference on*, oct. 2011, pp. 7 –12.

[3] K. Harada, S. Kajita, K. Kaneko, and H. Hirukawa, "Dynamics and balance of a humanoid robot during manipulation tasks," *IEEE Trans. Robot.*, vol. 22, no. 3, pp. 568–575, 2006.

[4] D. Mellinger, Q. Lindsey, M. Shomin, and V. Kumar, "Design, modeling, estimation and control for aerial grasping and manipulation," in *Proc. IEEE/RSJ Int Intelligent Robots and Systems (IROS) Conf*, 2011, pp. 2668–2673.

[5] P. E. I. Pounds, D. R. Bersak, and A. M. Dollar, "Grasping from the air: Hovering capture and load stability," in *Proc. IEEE Int Robotics and Automation (ICRA) Conf*, 2011, pp. 2491–2498.

[6] V. Ghadiok, J. Goldin, and W. Ren, "Autonomous indoor aerial gripping using a quadrotor," in *Intelligent Robots and Systems (IROS), 2011 IEEE/RSJ International Conference on*, sept. 2011, pp. 4645 – 4651.

[7] A. Keemink, M. Fumagalli, S. Stramigioli, and R. Carloni, "Mechanical design of a manipulation system for unmanned aerial vehicles," in *Robotics and Automation (ICRA), 2012 IEEE International Conference on*, may 2012, pp. 3147 –3152.

[8] I. Palunko, R. Fierro, and P. Cruz, "Trajectory generation for swing-free maneuvers of a quadrotor with suspended payload: A dynamic programming approach," in *Robotics and Automation (ICRA), 2012 IEEE International Conference on*, may 2012, pp. 2691 –2697.

[9] S. Bellens, J. De Schutter, and H. Bruyninckx, "A hybrid pose / wrench control framework for quadrotor helicopters," in *Robotics and Automation (ICRA), 2012 IEEE International Conference on*, may 2012, pp. 2269 –2274.

[10] A. Albers, S. Trautmann, T. Howard, T. A. Nguyen, M. Frietsch, and C. Sauter, "Semi-autonomous flying robot for physical interaction with environment," in *Robotics Automation and Mechatronics (RAM), 2010 IEEE Conference on*, june 2010, pp. 441 –446.

[11] www.airobots.eu.

[12] M. Orsag, C. Korpela, and P. Oh, "Modeling and control of MM-UAV: Mobile manipulating unmanned aerial vehicle," in *Proc.International Conference on Unmanned Aircraft Systems, ICUAS*, 2012.

[13] C. Korpela, M. Orsag, T. Danko, B. Kobe, C. McNeil, R. Pisch, and P. Oh, "Flight stability in aerial redundant manipulators," in *Proc. IEEE Int Robotics and Automation (ICRA) Conf*, 2012.

[14] S. McMillan, D. E. Orin, and R. B. McGhee, "Efficient dynamic simulation of an underwater vehicle with a robotic manipulator," *IEEE Transactions On Systems, Man, and Cybernetics*, vol. 25, pp. 1194–1206, 1995.

[15] H. Hahn, *Rigid Body Dynamics of Mechanisms: Theoretical basis*, ser. Rigid Body Dynamics of Mechanisms. Springer, 2002.

[16] M. P. Merchant, "Propeller performance measurement for low Reynolds number unmanned aerial vehicle applications," 2004.

[17] N. Miskovic, Z. Vukic, M. Bibuli, M. Caccia, and G. Bruzzone, "Marine vehicles' line following controller tuning through self-oscillation experiments," in *Proceedings of the 2009 17th Mediterranean Conference on Control and Automation*, ser. MED '09. Washington, DC, USA: IEEE Computer Society, 2009, pp. 916–921.

[18] P. I. Corke, *Robotics, Vision & Control: Fundamental Algorithms in Matlab*. Springer, 2011.